

Dispersion Analysis of the Discontinuous Enrichment Method for Plane-strain Elasticity

I. Harari & N. Makmel

To cite this article: I. Harari & N. Makmel (2009) Dispersion Analysis of the Discontinuous Enrichment Method for Plane-strain Elasticity, International Journal for Computational Methods in Engineering Science and Mechanics, 10:5, 303-316, DOI: [10.1080/15502280903023157](https://doi.org/10.1080/15502280903023157)

To link to this article: <https://doi.org/10.1080/15502280903023157>



Published online: 06 Aug 2009.



Submit your article to this journal [↗](#)



Article views: 66



View related articles [↗](#)

Dispersion Analysis of the Discontinuous Enrichment Method for Plane-strain Elasticity

I. Harari and N. Makmel

Faculty of Engineering, Tel Aviv University, Tel Aviv, Israel

We analyze the dispersion properties of plane-strain elements obtained by the discontinuous enrichment method (DEM). In DEM, the standard polynomial field is enriched within each element by a non-conforming field that is added to it. The dispersion analysis is performed on Lagrange multipliers, which weakly enforce the continuity of the solution and thus are associated with the inter-element traction. We use an eigenvalue-based procedure to compute the phase and polarization errors. The dispersion analysis is corroborated by results of numerical experiments.

Keywords Dispersion, Discontinuous enrichment method, Plane strain, Lagrange multipliers, Boundary traction, Polarization

1. INTRODUCTION

The time-harmonic elastic equation of motion represents vector-valued wave propagation problems. The purpose of analyzing wave problems is to compute the deformation and the distribution of stresses as functions of the spatial coordinates. Given the complicated geometry and the need to allow spatially varying elastic parameters, an obvious candidate for solving the elastic problem is the finite element method (FEM). The standard finite element method is based on the continuous, piecewise polynomial, Galerkin approximation (see, for example, [25]). However, the standard Galerkin method is computationally expensive and impractical for high frequency problems. Furthermore, using the standard Galerkin method, the error increases with the growth of the wave number, even if the number of elements per wavelength is kept constant [4]. This error was named pollution (or an accumulation of spurious dispersion) in [2].

Several techniques can be used to evaluate the numerical error of a given method. In the context of wave propagation problems, a widespread way to estimate the accuracy of the numerical solution is to examine the wave number and its polarization.

This error analysis is referred to as dispersion analysis (see, for example, [1, 8, 34]).

More than a few numerical methods have been proposed to reduce the pollution error in the context of the elastic problem. Inevitably, these are based on the standard piecewise polynomial Galerkin approximation. Among these approaches we note the stabilized methods Galerkin/least-squares [12] and Galerkin/gradient least-squares [19], variational multiscale methods [24, 26, 37], and residual-free bubbles (RFB) [11]. Approximation methods based on plane waves basis functions that better represent the oscillatory behavior of the wave field include the partition of unity method (PUM) [3, 33, 36], the ultra weak variational formulation (UWVF) [27, 28], and the variational theory of complex rays (VTCR) [31].

In this work the application of the Discontinuous Enrichment Method (DEM) for elastic waves is studied. DEM is an extended FEM that was introduced in [9] for the solution of problems with sharp gradients and rapid oscillations. The main purpose of this method is to attain high coarse-mesh accuracy. In DEM, the standard polynomial field is enriched within each element by a non-conforming field that is added to it. The enrichment contains free-space solutions of the homogeneous differential equation. These enrichments are easy to obtain, and are virtually independent of the element geometry and polynomial order. Thus, features of the differential equation are included in the approximation. Like PUM, the number of the homogeneous solutions is determined in advance. Like RFB, but in contrast to PUM, the enrichment is added to, rather than multiplied by, the polynomial field. DEM distinguishes itself from PUM and VTCR by its ability to evaluate analytically the mass and stiffness matrices resulting from the enrichment. This is a significant advantage for DEM as most enrichment functions require higher-order quadrature rules for evaluating the aforementioned matrices. This integration typically increases computational complexity and reduces robustness. The enrichment basis functions of DEM, which are usually easy to obtain analytically, are discontinuous across element interfaces. DEM relies on the Lagrange multipliers to enforce weak continuity of the solution at the element interfaces. In DEM, we expect to retain the high coarse mesh accuracy of PUM without significant

The authors wish to thank Paul Barbone, Ran Ganel, Eran Grosu, Shimon Shmulman, and Vitaly Skralivetsky for helpful discussions.

Address correspondence to Prof. Isaac Harari, Faculty of Engineering, Tel Aviv University, Tel Aviv 69978, Israel. E-mail: harari@eng.tau.ac.il

degradation of conditioning. Furthermore, due to the discontinuity of the enrichment across elements boundaries, the DEM formulation can be simplified and conditioned by means of static condensation. **The enrichment is defined within the element and thus can be eliminated from the formulation at the element level. As a result, the number of enrichment basis functions in the element has virtually no effect on the computational cost. The global coefficient matrix is reduced by this operation.**

The formulation of DEM in the context of the elastic problem is presented in [41], where high-order rectangular elements are proposed. In these high-order elements, the enrichment field is spanned by **up to 16 elastic plane waves in various directions** relative to the mesh. The Lagrange multipliers are also approximated by a superposition of pressure and shear plane waves. Attention is focused on the enrichment component and the corresponding space of Lagrange multipliers. Hence, the numerical evaluations are presented without considering the contribution of the polynomial part to the performance of the DEM element. DEM without its polynomial field was named Discontinuous Galerkin Method (DGM) [17], because of its discontinuous Galerkin aspects. For recent work on DEM in the context of fluid-solid problems see [35, 40].

In this paper, **we consider a DEM element in which the polynomial part is a standard finite element function defined by four-noded bilinear isoparametric interpolation. The enrichment part is spanned in each element by four pairs of longitudinal and transverse vector-valued, plane wave basis functions. The Lagrange multipliers are approximated by piecewise constants along the element sides.** The polynomial part is considered in the formulation of DEM, as well as in the numerical evaluations presented in this paper. The relative effect of the polynomial part on the entire DEM solution is quantified. In addition, a dispersion analysis for the proposed plane-strain DEM element is formulated and characterized.

The reminder of this paper is organized as follows. The formulation of DEM for the elastic wave problem is presented in Section 2. In Section 3 we introduce the plane-strain DEM element and the enrichment basis functions used in this element. The representation of the Lagrange multipliers related to the boundary traction is outlined. The dispersion analysis of DEM, performed on the Lagrange multipliers, is formulated and its results are presented. In Section 4, the performance of the plane-strain DEM elements is assessed and benchmarked against that of the standard Galerkin elements. The computational complexity of the DEM elements is addressed. Conclusions are offered in Section 5.

2. THE DISCONTINUOUS ENRICHMENT METHOD FOR TIME-HARMONIC ELASTIC WAVES

2.1. Boundary Value Problem for Time-Harmonic Elasticity

Let Ω be a region in d -dimensional space containing an elastic medium, bounded by an external boundary, Γ . For simplic-

ity, we consider the following Dirichlet boundary-value problem for the linear equation of motion: find $\mathbf{u} = \{u_i\}$, that satisfies:

$$\begin{aligned}\mathcal{L}\mathbf{u} &= \mathbf{f} \text{ in } \Omega \\ \mathbf{u} &= \mathbf{g} \text{ on } \Gamma,\end{aligned}\quad (2.1)$$

where $\mathcal{L}\mathbf{u} = -\text{div}\boldsymbol{\sigma} - \rho\omega^2\mathbf{u}$, $\boldsymbol{\sigma} = [\sigma_{ij}]$ is the stress tensor, ρ is the given mass density, ω is the given angular frequency, \mathbf{f} denotes the prescribed body forces or external loads, and \mathbf{g} are the prescribed boundary displacements on Γ . The method described herein applies to problems with other types of boundary conditions.

For a linear elastic medium, stress is defined in terms of strain by the generalized Hooke's law,

$$\sigma_{ij} = c_{ijkl}u_{(k,l)}. \quad (2.2)$$

The fourth-order tensor of elastic coefficients, $\mathbf{c} = [c_{ijkl}]$, satisfies the usual major and minor symmetry and positive-definiteness properties. The summation convention for repeated indices i, j, k, l is used from here on. The indices may take the values $1, \dots, d$, where d is the number of spatial dimensions. A comma indicates partial differentiation and:

$$u_{(i,j)} = \frac{1}{2}(u_{i,j} + u_{j,i}). \quad (2.3)$$

In an isotropic elastic medium, c_{ijkl} depend only on two parameters, for example the Lamé parameters, λ and μ . In this case, the elastic coefficients can be explicitly expressed for plane-strain ($d = 2$) and three-dimensional configurations ($d = 3$) as follows:

$$c_{ijkl} = \lambda\delta_{ij}\delta_{kl} + \mu(\delta_{ik}\delta_{jl} + \delta_{il}\delta_{jk}). \quad (2.4)$$

Here δ_{ij} is the Kronecker delta. The Lamé parameters, λ and μ , are related to Young's modulus, E , and Poisson ratio, ν , via

$$\mu = \frac{E}{2(1+\nu)}; \quad \lambda = \frac{\nu E}{(1+\nu)(1-2\nu)}. \quad (2.5)$$

The longitudinal and transverse wave numbers, k_L and k_T , respectively, are:

$$k_L = \sqrt{\frac{\rho\omega^2}{\lambda + 2\mu}}, \quad (2.6)$$

$$k_T = \sqrt{\frac{\rho\omega^2}{\mu}}. \quad (2.7)$$

The ratio of these wave numbers depends only on Poisson's ratio, ν , via equation (2.5):

$$\frac{k_T^2}{k_L^2} = \frac{2(1-\nu)}{1-2\nu} \equiv \tilde{\nu}. \quad (2.8)$$

Comparing the longitudinal wave number with the transverse wave number yields that in all cases of $0 \leq \nu < 1/2$,

$$k_T \geq \sqrt{2}k_L, \quad (2.9)$$

which indicates that the transverse wave number is larger than the longitudinal wave number.

A homogeneous isotropic plane elastic medium admits free-space homogeneous solutions in the form of longitudinal (pressure) and transverse (shear) plane waves, respectively:

$$\mathbf{u} = \begin{Bmatrix} \cos \theta \\ \sin \theta \end{Bmatrix} e^{ik_L(x \cos \theta + y \sin \theta)}, \quad (2.10)$$

$$\mathbf{u} = \begin{Bmatrix} -\sin \theta \\ \cos \theta \end{Bmatrix} e^{ik_T(x \cos \theta + y \sin \theta)}. \quad (2.11)$$

Here θ is the wave propagation angle with respect to the x -coordinate, and $i = \sqrt{-1}$ is the imaginary unit.

For homogeneous isotropic plane-strain, stress, $\boldsymbol{\sigma}$, is obtained by using the generalized Hooke's law, (2.2), and via the relation between strain to displacement, (2.3). We consider a displacement in the form of the longitudinal and transverse plane waves, (2.10) and (2.11). Stress is then represented in the following form, for the longitudinal and transverse waves, respectively:

$$\begin{aligned} \boldsymbol{\sigma} &= \tilde{\boldsymbol{\sigma}} e^{ik_L(x \cos \theta + y \sin \theta)}, \\ \boldsymbol{\sigma} &= \tilde{\boldsymbol{\sigma}} e^{ik_T(x \cos \theta + y \sin \theta)}. \end{aligned} \quad (2.12)$$

where:

$$\tilde{\boldsymbol{\sigma}} = \frac{i\rho\omega^2}{k_L} \begin{bmatrix} 1 - \frac{1}{\tilde{\nu}}(1 - \cos 2\theta) & \frac{1}{\tilde{\nu}} \sin 2\theta \\ \text{symm.} & 1 - \frac{1}{\tilde{\nu}}(1 + \cos 2\theta) \end{bmatrix}, \quad (2.13)$$

for the longitudinal wave, and:

$$\tilde{\boldsymbol{\sigma}} = \frac{i\rho\omega^2}{k_T} \begin{bmatrix} -\sin 2\theta & \cos 2\theta \\ \text{symm.} & \sin 2\theta \end{bmatrix}, \quad (2.14)$$

for the transverse wave.

The case of isotropic plane stress can be obtained by making the substitution:

$$\lambda \leftarrow \frac{2\lambda\mu}{\lambda + 2\mu} = \frac{\nu E}{1 - \nu^2}. \quad (2.15)$$

Accordingly, the ratio between the wave velocities for the plane stress case, via equation (2.2), is

$$\frac{k_T^2}{k_L^2} = \frac{2}{1-\nu}. \quad (2.16)$$

2.2. Discretization by the Discontinuous Enrichment Method

The following presentation of the Discontinuous Enrichment Method (DEM) is based on References [9] and [41]. Consider a partition of Ω , the computational domain, into n_{el} non-overlapping finite element domains Ω^e , ($e = 1, \dots, n_{el}$), with element boundaries Γ^e . Let $\tilde{\Omega}$ be the union of element interiors, and $\tilde{\Gamma}$, the union of element boundaries,

$$\tilde{\Omega} = \bigcup_{e=1}^{n_{el}} \Omega^e; \quad \tilde{\Gamma} = \bigcup_{e=1}^{n_{el}} \Gamma^e. \quad (2.17)$$

The element interfaces or interior element boundaries are defined by $\Gamma_{\text{int}} = \tilde{\Gamma} \setminus \Gamma$.

2.2.1. Variational Formulation

The variational form of the boundary-value problem (2.1) is stated in terms of trial solutions that may be discontinuous across element boundaries. Similarly, these solutions are not required to satisfy Dirichlet boundary conditions. Inter-element continuity and Dirichlet boundary conditions are both enforced weakly by Lagrange multipliers, denoted by $\boldsymbol{\lambda}$.

Let \mathbf{v} be an arbitrary variation of \mathbf{u} . Allowing for discontinuities, we define the bilinear operator over element interiors, $\tilde{\Omega}$, as follows:

$$a(\mathbf{v}, \mathbf{u}) = (\nabla \mathbf{v}, \mathbf{c} \nabla \mathbf{u})_{\tilde{\Omega}} - \omega^2(\mathbf{v}, \rho \mathbf{u}). \quad (2.18)$$

Here, the domain and boundary integration are given in terms of the operators:

$$(\mathbf{v}, \mathbf{u}) = \int_{\Omega} \mathbf{v} \cdot \mathbf{u} \, d\Omega \quad \langle \boldsymbol{\lambda}, \mathbf{v} \rangle = \int_{\Gamma} \mathbf{v} \boldsymbol{\lambda} \, d\Gamma, \quad (2.19)$$

for continuous functions, and:

$$(\mathbf{v}, \mathbf{u})_{\tilde{\Omega}} = \int_{\tilde{\Omega}} \mathbf{v} \cdot \mathbf{u} \, d\Omega \quad \langle \boldsymbol{\lambda}, \mathbf{v} \rangle_{\tilde{\Gamma}} = \int_{\tilde{\Gamma}} \mathbf{v} \boldsymbol{\lambda} \, d\Gamma, \quad (2.20)$$

for discontinuous functions.

Let $\boldsymbol{\mu}$ be arbitrary variation of $\boldsymbol{\lambda}$. The objective is to find the trial solution, \mathbf{u} , such that for all weighting functions, \mathbf{v} :

$$\begin{aligned} a(\mathbf{v}, \mathbf{u}) - \langle \boldsymbol{\lambda}, [\![\mathbf{v}]\!] \rangle_{\tilde{\Gamma}} &= (\mathbf{v}, \mathbf{f}) \\ - \langle \boldsymbol{\mu}, [\![\mathbf{u}]\!] \rangle_{\tilde{\Gamma}} &= - \langle \boldsymbol{\mu}, \mathbf{g} \rangle. \end{aligned} \quad (2.21)$$

Here, $\llbracket \mathbf{u} \rrbracket$ denotes the jump in \mathbf{u} . The first of Equations (2.21) is an element-by-element weak form of the governing equation of motion. The second of these equations is a weak form of the displacement continuity across the element boundaries. The corresponding Euler-Lagrange equations are:

$$\begin{aligned} \mathcal{L}\mathbf{u} &= \mathbf{f} \quad \text{in } \tilde{\Omega}, \\ \llbracket \mathbf{u} \rrbracket &= \mathbf{0} \quad \text{on } \Gamma_{\text{int}}, \\ \mathbf{u} &= \mathbf{g} \quad \text{on } \Gamma, \\ \boldsymbol{\lambda} &= \boldsymbol{\sigma} \cdot \mathbf{n} \quad \text{on } \tilde{\Gamma}. \end{aligned} \quad (2.22)$$

Since the Lagrange multiplier weakly enforces the continuity between the elements, its Euler-Lagrange equation presented in (2.22) has the form of boundary traction.

2.2.2. Galerkin Approximation

In the Galerkin approximation of DEM, the trial solution, \mathbf{u}^h , is defined as the sum of a standard continuous piece-wise polynomial finite element function \mathbf{u}^P (coarse scale) and an enrichment field \mathbf{u}^E (fine scale) [9]:

$$\mathbf{u}^h = \mathbf{u}^P + \mathbf{u}^E. \quad (2.23)$$

The approximate solution is related to the typical element size, h .

The polynomial part of DEM is continuous between the elements, while the enrichment field may be discontinuous across element boundaries. The enrichment field, which is defined inside each element separately, satisfies the free-space homogeneous equation of motion:

$$\mathcal{L}\mathbf{u}^E = \mathbf{0} \quad \text{in } \mathbb{R}^d. \quad (2.24)$$

The Galerkin approximation is expressed in terms of weighting functions for the polynomials, \mathbf{v}^P , enrichment weighting functions, \mathbf{v}^E , and Lagrange multiplier weighting functions, $\boldsymbol{\mu}^h$. The decomposed Galerkin approximation has the following form [9]:

$$\begin{aligned} a(\mathbf{v}^P, \mathbf{u}^P) + a(\mathbf{v}^P, \mathbf{u}^E) - \langle \boldsymbol{\lambda}^h, \mathbf{v}^P \rangle &= (\mathbf{v}^P, \mathbf{f}) \\ a(\mathbf{v}^E, \mathbf{u}^P) + a(\mathbf{v}^E, \mathbf{u}^E) - \langle \boldsymbol{\lambda}^h, \llbracket \mathbf{v}^E \rrbracket \rangle_{\tilde{\Gamma}} &= (\mathbf{v}^E, \mathbf{f}) \\ -\langle \boldsymbol{\mu}^h, \mathbf{u}^P \rangle - \langle \boldsymbol{\mu}^h, \llbracket \mathbf{u}^E \rrbracket \rangle_{\tilde{\Gamma}} &= -\langle \boldsymbol{\mu}^h, \mathbf{g} \rangle. \end{aligned} \quad (2.25)$$

2.3. Matrix Form

Following [9], the partitioned matrix form of the global system of discrete equations defined in (2.25) is:

$$\begin{bmatrix} \mathbf{K}^{PP} & \mathbf{K}^{PE} & \mathbf{K}^{PC} \\ \mathbf{K}^{EP} & \mathbf{K}^{EE} & \mathbf{K}^{EC} \\ \mathbf{K}^{CP} & \mathbf{K}^{CE} & \mathbf{0} \end{bmatrix} \begin{Bmatrix} \mathbf{u}^P \\ \mathbf{u}^E \\ \boldsymbol{\lambda}^h \end{Bmatrix} = \begin{Bmatrix} \mathbf{F}^P \\ \mathbf{F}^E \\ \mathbf{F}^C \end{Bmatrix}. \quad (2.26)$$

The superscript letters in the matrices stand for P for polynomials, E for the enrichment functions, and C for the constraint

field. The correspondence between the global matrices and the terms in the Galerkin equation, (2.25), is presented in [9] and [41]. The formulation can be simplified and conditioned by means of static condensation [9]. This is due to the enrichment being defined within the element, which allows the enrichment to be eliminated from the formulation on the element level. As a result, **the number of enrichment basis functions in the element has virtually no effect on the computational cost.** The global coefficient matrix is reduced by this operation.

In order to define the static condensation mathematically, let \mathbf{k} and \mathbf{f} be the element coefficient matrix and load vector, respectively, where \mathbf{K} and \mathbf{F} stand for global coefficient matrix and load vector. Local and global coefficient matrices have the same form and both are constructed from nine sub-matrices, see (2.26). On the element level, the following equation expresses the local enrichment degrees of freedom, \mathbf{u}^E , in terms of \mathbf{u}^P and $\boldsymbol{\lambda}^h$ (the polynomial and the Lagrange multiplier degrees of freedom, respectively):

$$\mathbf{u}^E = (\mathbf{k}^{EE})^{-1}(\mathbf{f}^E - \mathbf{k}^{EP}\mathbf{u}^P - \mathbf{k}^{EC}\boldsymbol{\lambda}^h). \quad (2.27)$$

For each element, the formulation is reduced from three fields to two. The enrichment degrees of freedom are eliminated on the element level and the following coefficient matrix is obtained:

$$\tilde{\mathbf{k}}^e = \begin{bmatrix} \tilde{\mathbf{k}}^{PP} & \tilde{\mathbf{k}}^{PC} \\ \tilde{\mathbf{k}}^{CP} & \tilde{\mathbf{k}}^{CC} \end{bmatrix}, \quad (2.28)$$

where the condensed matrices are obtained as follows:

$$\begin{aligned} \tilde{\mathbf{k}}^{PP} &= \mathbf{k}^{PP} - \mathbf{k}^{PE}(\mathbf{k}^{EE})^{-1}\mathbf{k}^{EP} \\ \tilde{\mathbf{k}}^{PC} &= \mathbf{k}^{PC} - \mathbf{k}^{PE}(\mathbf{k}^{EE})^{-1}\mathbf{k}^{EC} \\ \tilde{\mathbf{k}}^{CP} &= \mathbf{k}^{CP} - \mathbf{k}^{CE}(\mathbf{k}^{EE})^{-1}\mathbf{k}^{EP} \\ \tilde{\mathbf{k}}^{CC} &= -\mathbf{k}^{CE}(\mathbf{k}^{EE})^{-1}\mathbf{k}^{EC}, \end{aligned} \quad (2.29)$$

and the element-level load vectors associated with the matrix coefficients of (2.28) are:

$$\begin{aligned} \tilde{\mathbf{f}}^P &= \mathbf{f}^P - \mathbf{k}^{PE}(\mathbf{k}^{EE})^{-1}\mathbf{f}^E \\ \tilde{\mathbf{f}}^C &= \mathbf{f}^C - \mathbf{k}^{CE}(\mathbf{k}^{EE})^{-1}\mathbf{f}^E. \end{aligned} \quad (2.30)$$

Assembling of the element-level condensed matrices leads to the following alternative form of the algebraic problem (2.26):

$$\begin{bmatrix} \tilde{\mathbf{K}}^{PP} & \tilde{\mathbf{K}}^{PC} \\ \tilde{\mathbf{K}}^{CP} & \tilde{\mathbf{K}}^{CC} \end{bmatrix} \begin{Bmatrix} \mathbf{u}^P \\ \boldsymbol{\lambda}^h \end{Bmatrix} = \begin{Bmatrix} \tilde{\mathbf{F}}^P \\ \tilde{\mathbf{F}}^C \end{Bmatrix}. \quad (2.31)$$

Here, the load vectors $\tilde{\mathbf{F}}^P$ and $\tilde{\mathbf{F}}^C$, which are related to the polynomial and the constraint fields, respectively, are the assembled counterparts of the element-level quantities defined in (2.30).

3. PLANE-STRAIN ELEMENT AND DISPERSION ANALYSIS

3.1. Basic Element



The DEM solution consists of two parts: a polynomial part and an enrichment part (2.23). The polynomial part is a standard finite element function defined by four-noded bilinear isoparametric interpolation. The enrichment part is spanned in each element by a number of vector-valued, complex, longitudinal and transverse plane wave basis functions, see (2.10) and (2.11). These functions satisfy the free-space homogeneous isotropic elastic equation. It should be noted that with the polynomial part of the approximation, the different components of the displacement vector are discretized independently, while the vector-valued plane-wave approximation discretizes the components in a consistent fashion. Generally, different combinations of plane wave basis functions can be applied to the enrichment field. The basis functions are different one from the other in terms of the propagation orientation angle, θ .

To simplify the analysis, the complex-valued exponential functions can be replaced by real-valued trigonometric functions, if the enrichment is spanned by an even number of plane waves. The use of these trigonometric functions leads to real coefficient matrices on the element level.

The basic plane-strain DEM element is presented in Figure 1. The polynomial part of this element is defined by standard bilinear nodal basis functions and is shown by four points in the figure. The enrichment of the basic element is spanned by eight vector-valued functions corresponding to four pairs of longitudinal and transverse plane waves propagating along the axes and is defined in the parent domain (bi-unit square in natural coordinates) of a square element. The arrows in Figure 1 represent the longitudinal and transverse plane wave basis functions and are pointing at the directions of the plane wave propagation. The boundary tractions related to the plane waves in the enrichment field vary along element edges. However, the Lagrange multipliers can be approximated by piecewise constants along the element sides. Consequently, every edge has one vector-valued

degree of freedom. The piecewise constant Lagrange multipliers of the element are marked in Figure 1 along the element edges by lines.

3.2. Dispersion for the Plane-strain DEM Element

3.2.1. Dispersion Procedure for DEM

The dispersion analysis for DEM is performed by a special procedure. First, the enrichment is eliminated from the formulation by static condensation at the element level, as described earlier. The two remaining fields, the polynomial and constraint, are coupled but the coupling is weak.

Dispersion analysis of the polynomial solution does not fill a central role in the context of DEM, since the dispersion analysis characterizes homogeneous frequency-dependent solutions. The polynomials, however, represent the particular solutions (coarse scales) [10]. These solutions are not associated with the frequency response of the problem but with the problem's data. Furthermore, a dispersion analysis for acoustics, presented in [9], shows strong damping of the polynomial field. As a result, the constraint field remains the only part for which dispersion analysis is relevant. This claim will be also backed up by numerical tests in Section 4, where we show a correlation between the performance of the constraint and the displacement fields. The constraint field is represented through the Lagrange multipliers, which enforce continuity. Therefore, the performance of the DEM element is represented by the dispersion properties of the Lagrange multipliers.

The Lagrange multipliers represent boundary tractions that enforce the continuity of the numerical solution, see (2.22). These Lagrange multipliers are defined on the element boundaries and therefore must be analyzed differently than the nodal degrees of freedom of the polynomials.

3.2.2. Stencil for the Plane-strain Element

The goal is to define a general pattern within the mesh, from which the dispersion properties can be studied. Recall that when using constant Lagrange multipliers we have one vector-valued degree of freedom for each element boundary. The Lagrange multipliers enforce the continuity of the numerical solution between two neighboring elements. Therefore, we consider a stencil that connects two elements with one common Lagrange multiplier on their mutual boundary. A combination of two vector-valued stencils, perpendicular to each other, as shown in Figure 2, enables us to include in the dispersion analysis a contribution of two kinds of vector-valued Lagrange multipliers. One of these Lagrange multipliers is related to a horizontal edge, and the other is related to a vertical edge. Each of the stencils yields two equations, one equation for each component of the vector-valued Lagrange multiplier. Thus, the total number of equations that are obtained from these two vector-valued stencils is four.

3.2.3. Dispersion Analysis of the Plane-strain Element

As in typical dispersion analyses, the mesh is aligned with the global axes. We associate edge values of the piecewise

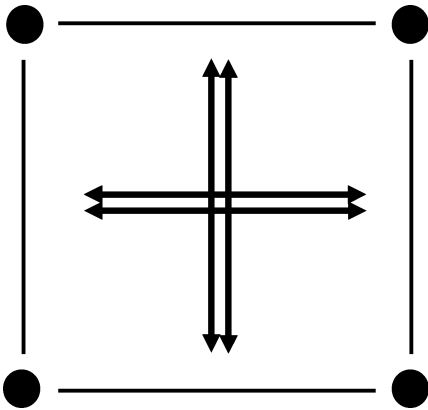


FIG. 1. Basic plane-strain DEM element.

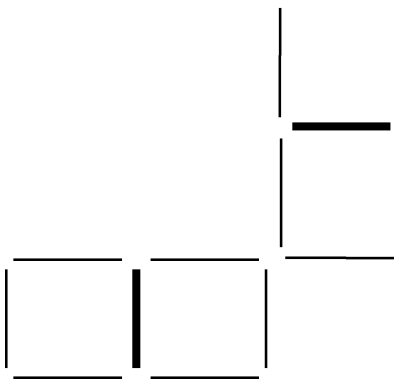


FIG. 2. A combination of two vector-valued stencils perpendicular to each other.

constant Lagrange multipliers with the middle of each edge (Figure 3).

We consider a uniform mesh of elements of size h , with vertices at $\mathbf{x}_A = (mh, nh)$, $m, n \in \mathbb{Z}$. The Lagrange multipliers are associated with the boundary traction, obtained from the stress. We define stress related to the constraint field in the following plane wave form, which is based on the exact plane wave stress (2.12):

$$\boldsymbol{\sigma}^C(\mathbf{x}_A) = \tilde{\boldsymbol{\sigma}}^C(e^{ik^C h \cos \theta})^m (e^{ik^C h \sin \theta})^n, \quad (3.1)$$

where:

$$\tilde{\boldsymbol{\sigma}}^C = \begin{bmatrix} \tilde{\sigma}_{xx}^C & \tilde{\sigma}_{xy}^C \\ \tilde{\sigma}_{yx}^C & \tilde{\sigma}_{yy}^C \end{bmatrix}. \quad (3.2)$$

This stress is expressed in terms of the unknown amplitudes, $\tilde{\boldsymbol{\sigma}}^C$, multiplied by plane waves with the unknown approximate wave number, k^C , associated with the constraint field. Note that no symmetry of $\boldsymbol{\sigma}^C$ is assumed in advance. The representation of the Lagrange multipliers at the relevant points on the edges is then given in the following form, which is based on (3.1):

$$\boldsymbol{\lambda}^h(\mathbf{x}_A) = \tilde{\boldsymbol{\sigma}}^C(e^{ik^C h \cos \theta})^m (e^{ik^C h \sin \theta})^n \cdot \mathbf{n}, \quad (3.3)$$

where \mathbf{n} denotes the outward unit vector normal to the element boundary.

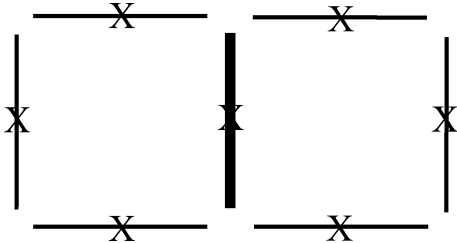


FIG. 3. A seven edge stencil. The piecewise constant edge values are associated with the middle of each edge and are marked by X.

After static condensation, the corresponding 8×8 matrix, $\tilde{\mathbf{k}}^{CC}$, see (2.29), is:

$$\tilde{\mathbf{k}}^{CC} = \frac{1}{\rho\omega^2} \begin{bmatrix} a_1 & -1 & a_2 & 1 & 0 & a_3 & 0 & a_3 \\ -1 & a_4 & 1 & a_5 & a_6 & 0 & a_6 & 0 \\ a_2 & 1 & a_1 & -1 & 0 & a_3 & 0 & a_3 \\ 1 & a_5 & -1 & a_4 & a_6 & 0 & a_6 & 0 \\ 0 & a_6 & 0 & a_6 & a_4 & -1 & a_5 & 1 \\ a_3 & 0 & a_3 & 0 & -1 & a_1 & 1 & a_2 \\ 0 & a_6 & 0 & a_6 & a_5 & 1 & a_4 & -1 \\ a_3 & 0 & a_3 & 0 & 1 & a_2 & -1 & a_1 \end{bmatrix} \quad (3.4)$$

where the terms of (3.4) are defined as follows:

$$\begin{aligned} a_1 &= \frac{2v_3^2 - v_{1L}(v_{1L} + v_{2L})}{(v_{1L} - v_{2L})[(v_{1L} + v_{2L})^2 - 4v_3^2]} \\ a_2 &= \frac{v_{2L}(v_{1L} + v_{2L}) - 2v_3^2}{(v_{1L} - v_{2L})[(v_{1L} + v_{2L})^2 - 4v_3^2]} \\ a_3 &= \frac{v_3}{(v_{1L} + v_{2L})^2 - 4v_3^2} \\ a_4 &= \frac{2v_4^2 - v_{1T}(v_{1T} + v_{2T})}{(v_{1T} - v_{2T})[(v_{1T} + v_{2T})^2 - 4v_4^2]} \\ a_5 &= \frac{v_{2T}(v_{1T} + v_{2T}) - 2v_4^2}{(v_{1T} - v_{2T})[(v_{1T} + v_{2T})^2 - 4v_4^2]} \\ a_6 &= \frac{v_4}{(v_{1T} + v_{2T})^2 - 4v_4^2}. \end{aligned} \quad (3.5)$$

Here, the terms of (3.5) are defined via the following trigonometric functions, with the longitudinal and the transverse wave numbers, k_L and k_T , respectively, and the mesh parameter, h :

$$\begin{aligned} v_{1L} &= \frac{\cos(k_L h)}{k_L h \sin(k_L h)} & v_{2L} &= \frac{1}{k_L h \sin(k_L h)} \\ v_{1T} &= \frac{\cos(k_T h)}{k_T h \sin(k_T h)} & v_{2T} &= \frac{1}{k_T h \sin(k_T h)} \\ v_3 &= v_{2L}^2 - v_{1L}^2 - 2(v_{2T}^2 - v_{1T}^2) = \frac{1}{(k_L h)^2} - \frac{2}{(k_T h)^2} \\ v_4 &= v_{2T}^2 - v_{1T}^2 = \frac{1}{(k_T h)^2}. \end{aligned} \quad (3.6)$$

In the single stencil of Figure 3 we consider the relation between the vector-valued degree of freedom, which is placed on the central edge, and the remaining six vector-valued degrees of freedom in the stencil. In the dispersion equation, these degrees of freedom are related to the center of each edge and are written in the form of the boundary traction, see (3.3). The dispersion equations are obtained by a multiplication of the matrix variables of (3.4) by the stencil's degrees of freedom.

In order to demonstrate the derivation of these dispersion equations, consider a single stencil, constructed of two elements as shown in Figure 4. The representation of the vector-valued

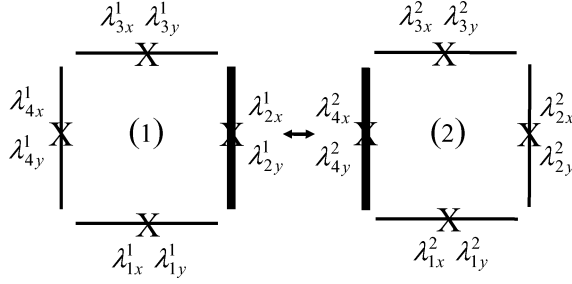


FIG. 4. Components of the Lagrange multipliers degrees of freedom, single stencil.

Lagrange multipliers is given by the components, λ_{Ai}^e , where e denotes the element number, i denotes the spatial direction, and A is the middle edge associated with the relevant Lagrange multiplier.

For each of the elements, the numbering of the Lagrange multipliers components is defined in Table 1.

In the x -direction, the Lagrange multiplier degree of freedom that connects the two elements corresponds to λ_{2x}^1 and λ_{4x}^2 , which are numbered as λ_2^1 and λ_4^2 , respectively. As a result, the dispersion equation in the x -direction of the considered stencil is derived by multiplying the second row variables of $\tilde{\mathbf{k}}^{CC}$ with

$$\mathbf{A}^C = \frac{1}{\rho\omega^2} \begin{bmatrix} a_2 \cos(k^C hC) + a_1 & 0 \\ a_5 \cos(k^C hC) + a_4 & \\ \text{symm.} & \end{bmatrix}$$

the first element degrees of freedom, and by multiplying the fourth row variables of $\tilde{\mathbf{k}}^{CC}$ with the second element degrees of freedom. This leads to the following dispersion equation:

$$\sum_{A=1}^8 k_{2,A}^{CC} \lambda_A^1 + \sum_{A=1}^8 k_{4,A}^{CC} \lambda_A^2 = 0. \quad (3.7)$$

In the y -direction, the Lagrange multiplier degree of freedom that connects the two elements corresponds to λ_{2y}^1 and λ_{4y}^2 , associated with the sixth and eighth rows of $\tilde{\mathbf{k}}^{CC}$. This leads to the second dispersion equation of the considered stencil:

$$\sum_{A=1}^8 k_{6,A}^{CC} \lambda_A^1 + \sum_{A=1}^8 k_{8,A}^{CC} \lambda_A^2 = 0. \quad (3.8)$$

In a similar way, another vector-valued stencil, perpendicular to the stencil of Figure 4, yields two additional dispersion

equations. Consequently, the total number of equations that are obtained from the two stencils combination shown in Figure 2 is four. Each one of the stencils yields two equations: one equation for each component of a $2d$ vector-valued Lagrange multiplier, which is related to a shared boundary of two adjacent elements. However, the objective is to attain only one single dispersion equation from which we can get the relation between the approximate, Lagrange multipliers related, wave number, k^C , and the prescribed longitudinal and transverse wave numbers, k_L and k_T , respectively. The four equations that are received from the above-mentioned two stencils combination may be presented in the following form:

$$\mathbf{A}^C \begin{Bmatrix} \tilde{\sigma}_{xx}^C \\ \tilde{\sigma}_{yx}^C \\ \tilde{\sigma}_{xy}^C \\ \tilde{\sigma}_{yy}^C \end{Bmatrix} = \mathbf{0}. \quad (3.9)$$

This is a set of homogeneous linear algebraic equations for the unknown amplitudes, $\tilde{\sigma}_{xx}^C$, $\tilde{\sigma}_{yx}^C$, $\tilde{\sigma}_{xy}^C$ and $\tilde{\sigma}_{yy}^C$. The matrix \mathbf{A}^C is related to the constraint field and represented by the terms of the condensed matrix, $\tilde{\mathbf{k}}^{CC}$, see (3.4)–(3.6):

$$\begin{bmatrix} 2S_C S_S & 2a_3 C_C C_S \\ 2a_6 C_C C_S & 2S_C S_S \\ a_5 \cos(k^C hS) + a_4 & 0 \\ 0 & a_2 \cos(k^C hS) + a_1 \end{bmatrix} \quad (3.10)$$

where $S \equiv \sin \theta$, $C \equiv \cos \theta$, and:

$$\begin{aligned} S_C &= \sin(k^C hC/2) & S_S &= \sin(k^C hS/2) \\ C_C &= \cos(k^C hC/2) & C_S &= \cos(k^C hS/2). \end{aligned} \quad (3.11)$$

Nontrivial solutions of (3.9) exist when the coefficient matrix, \mathbf{A}^C , is singular (i.e., when the determinant vanishes). The resulting characteristic equation is a dispersion relation between the constraint field wave number, k^C , and the given longitudinal and transverse wave numbers, k_L and k_T , respectively. The dispersion equation for the plane-strain DEM element is presented in the following form:

$$(b_5 - r_1)(b_5 - r_2) = 0, \quad (3.12)$$

where:

$$\begin{aligned} r_1 &= \frac{b_2^2 b_3 - \left[(b_1 b_7 b_6 - b_2^2 b_7 - b_3^2 b_6) (b_1 b_7 b_4 - b_2^2 b_1 - b_3^2 b_4) \right]^{1/2}}{b_3^2 - b_1 b_7}, \\ r_2 &= \frac{b_2^2 b_3 + \left[(b_1 b_7 b_6 - b_2^2 b_7 - b_3^2 b_6) (b_1 b_7 b_4 - b_2^2 b_1 - b_3^2 b_4) \right]^{1/2}}{b_3^2 - b_1 b_7}, \end{aligned} \quad (3.13)$$

TABLE 1

Numbering of the element Lagrange multiplier degrees of freedom, single stencil

Element DOF's	λ_{1x}^e	λ_{2x}^e	λ_{3x}^e	λ_{4x}^e	λ_{1y}^e	λ_{2y}^e	λ_{3y}^e	λ_{4y}^e
DOF's numbering	λ_1^e	λ_2^e	λ_3^e	λ_4^e	λ_5^e	λ_6^e	λ_7^e	λ_8^e

and:

$$\begin{aligned} b_1 &= a_2 \cos(k^C h C) + a_1 & b_2 &= 2S_C S_S \\ b_3 &= 2a_3 C_C C_S & b_4 &= a_5 \cos(k^C h C) + a_4 \\ b_5 &= 2a_6 C_C C_S & b_6 &= a_5 \cos(k^C h S) + a_4 \\ b_7 &= a_2 \cos(k^C h S) + a_1 . \end{aligned} \quad (3.14)$$

Here, the expressions of (3.14) are presented in terms of the matrix \mathbf{A}^C of (3.10). The DEM dispersion equation is an implicit representation of the constraint field wave number, k^C . This dispersion relation is dependent on the orientation angle, θ , on the Poisson's ratio, ν , and on the wave resolution, $G = 2\pi/(kh)$, which is the number of nodal points per wavelength. The dispersion equation is solved numerically and its results are shown in Figures 5 and 6. In these figures, k_L^C and k_T^C denote the approximate longitudinal and transverse wave numbers associated with the constraint field. The other solutions of the characteristic equation associated with the coefficient matrix, \mathbf{A}^C , lead to complex-valued wave numbers. We will not refer to these complex-valued wave numbers in this paper.

The dispersion behavior of the constraint field is cyclic around $\theta = 90^\circ$ and symmetric with respect to $\theta = 45^\circ$. When the mesh is aligned with the wave (i.e., $\theta = 0^\circ$), the Lagrange multipliers are free of dispersion at all resolutions for any value of the Poisson's ratio, ν . The constraint field exhibits excellent dispersion properties at angles up to 10° from the direction of any of the enrichment's eight vector-valued plane waves at all resolutions. The accuracy of either longitudinal or transverse wave numbers deteriorates as θ increases, but yet there are good dispersion properties at any angle for the lowest resolution shown ($G = 4$ points per wavelength). The accuracy of the longitudinal wave number deteriorates as the Poisson's ratio, ν , increases, while the transverse wave number accuracy improves with the growth of ν .

equation, (3.12), in terms of (3.5) is:

$$\begin{aligned} &\{(2a_2(a_1 + a_2) - 4a_3^2) \cos^2(k^C h/2) - (a_2^2 - a_1^2)\} \\ &\{(2a_5(a_4 + a_5) - 4a_6^2) \cos^2(k^C h/2) - (a_5^2 - a_4^2)\} = 0 . \end{aligned} \quad (3.15)$$

The solutions of this dispersion equation are:

$$\begin{aligned} \cos^2(k^C h/2) &= \frac{a_2^2 - a_1^2}{2a_2(a_1 + a_2) - 4a_3^2} = \frac{v_{1L} + v_{2L}}{2v_{2L}} \\ &= \cos^2(k_L h/2) \Leftrightarrow k^C = k_L , \end{aligned} \quad (3.16)$$

and:

$$\begin{aligned} \cos^2(k^C h/2) &= \frac{a_5^2 - a_4^2}{2a_5(a_4 + a_5) - 4a_6^2} = \frac{v_{1T} + v_{2T}}{2v_{2T}} \\ &= \cos^2(k_T h/2) \Leftrightarrow k^C = k_T . \end{aligned} \quad (3.17)$$

Negative values of k^C in (3.16) and (3.17) merely correspond to propagation in the direction $\theta + 180^\circ$.

For $\theta = 45^\circ$, the following equation is obtained using the terms of (3.5):

$$\begin{aligned} &\{[1 - (a_5 - a_6)(a_2 - a_3)]r^2 - \\ &- [2 + (a_1 - a_3)(a_5 - a_6) + (a_4 - a_6)(a_2 - a_3)]r + \\ &+ [1 - (a_1 - a_3)(a_4 - a_6)]\} \{[1 - (a_5 + a_6)(a_2 + a_3)]r^2 - \\ &- [2 + (a_1 + a_3)(a_5 + a_6) + (a_4 + a_6)(a_2 + a_3)]r + \\ &+ [1 - (a_1 + a_3)(a_4 + a_6)]\} = \\ &= \{(r - 1)^2 - [(a_5 - a_6)r + (a_4 - a_6)][(a_2 - a_3)r + (a_1 - a_3)]\} \\ &\{(r - 1)^2 - [(a_5 + a_6)r + (a_4 + a_6)][(a_2 + a_3)r + (a_1 + a_3)]\} = 0 , \end{aligned} \quad (3.18)$$

where,

$$r \equiv \cos(k^C h \sqrt{2}/2) . \quad (3.19)$$

The solutions of this equation are:

$$\begin{aligned} k^C h &= \sqrt{2} \cos^{-1} \left(\frac{2 + (a_1 - a_3)(a_5 - a_6) + (a_4 - a_6)(a_2 - a_3)}{2(1 - (a_5 - a_6)(a_2 - a_3))} + \right. \\ &\quad \left. + \frac{\sqrt{\{(a_1 - a_3)(a_5 - a_6) - (a_2 - a_3)(a_4 - a_6)\}^2 + 4(a_1 + a_2 - 2a_3)(a_4 + a_5 - 2a_6)}}{2(1 - (a_5 - a_6)(a_2 - a_3))} \right) , \end{aligned} \quad (3.20)$$

which is a real-valued solution of the transverse wave number, k_T^C , associated with the constraint field, and:

$$\begin{aligned} k^C h &= \sqrt{2} \cos^{-1} \left(\frac{2 + (a_1 + a_3)(a_5 + a_6) + (a_4 + a_6)(a_2 + a_3)}{2(1 - (a_5 + a_6)(a_2 + a_3))} - \right. \\ &\quad \left. - \frac{\sqrt{\{(a_1 + a_3)(a_5 + a_6) - (a_2 + a_3)(a_4 + a_6)\}^2 + 4(a_1 + a_2 + 2a_3)(a_4 + a_5 + 2a_6)}}{2(1 - (a_5 + a_6)(a_2 + a_3))} \right) , \end{aligned} \quad (3.21)$$

We confirm these results by comparison to analytical expressions at the extreme angles. For $\theta = 0^\circ$, the characteristic

which is a complex-valued solution of the transverse wave number, k_T^C . Similarly, two other solutions corresponding to

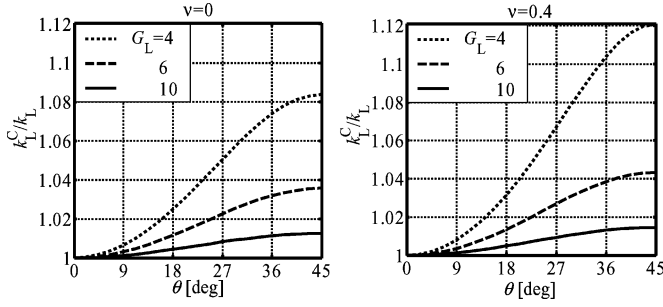


FIG. 5. Longitudinal phase error of the plane-strain DEM element.

real-valued and complex-valued representations of the longitudinal wave number, k_L^C , associated with the constraint field can be obtained. The results presented in Figures 5 and 6 comply with the analytical solution at these extreme angles.

The abovementioned dispersion results can be presented by means of convergence rate, which describes how the dispersion decreases as the mesh resolution is increased or as the frequency is reduced. The dispersion convergence rates for the longitudinal and transverse waves are presented in Figures 7 and 8, respectively.

The dispersion of the constraint field exhibits good convergence properties even at the largest angular deviation of the mesh relative to the wave (i.e., $\theta = 45^\circ$). For all the considered cases, the dispersion is found to be less than 7% for resolutions larger than 5 nodal points per wavelength, and less than 2% for resolutions larger than 10 nodal points per wavelength. The convergence results presented in Figures 7 and 8 correspond to the dispersion results presented in Figures 5 and 6.

In order to complete the picture, we consider the polarization error in addition to the phase error. We define the polarization error of the constraint field as the deviation between the amplitude tensors $\tilde{\sigma}$ and $\tilde{\sigma}^C$, associated with the exact and the assumed stresses, respectively, see (2.12) and (3.1). The polarization error is computed via the inner product of these tensor amplitudes and is defined as follows:

$$\phi^C = \cos^{-1} \left(\frac{\tilde{\sigma} : \tilde{\sigma}^C}{\|\tilde{\sigma}\|_F \|\tilde{\sigma}^C\|_F} \right). \quad (3.22)$$

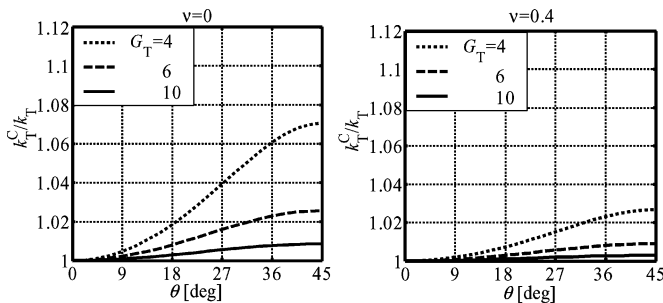


FIG. 6. Transverse phase error of the plane-strain DEM element.

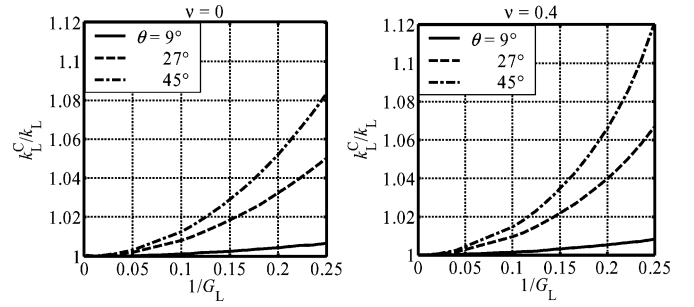


FIG. 7. Convergence rate, longitudinal phase error of the plane-strain DEM element.

Here, ϕ^C is the polarization error associated with the constraint field, $\tilde{\sigma} : \tilde{\sigma}^C = \text{trace}(\tilde{\sigma}^T \tilde{\sigma}^C)$ denotes the tensor inner product, and $\|\cdot\|_F$ is the Frobenius norm. Recall that the condition for nontrivial solutions to the homogeneous linear algebraic equations, (3.9), provides the constraint field wave numbers, k^C . However, substitution of the solutions for k^C in (3.9) leads to a linear dependency between the amplitudes, $\tilde{\sigma}_{xx}^C, \tilde{\sigma}_{yy}^C, \tilde{\sigma}_{xy}^C$ and $\tilde{\sigma}_{yx}^C$. The amplitude tensor, $\tilde{\sigma}^C$, is found up to a multiplicative constant. This is sufficient in order to determine the polarization error. The polarization error (3.22) is valid for either longitudinal or transverse waves. For the case of the longitudinal wave, the constraint field wave number, k^C , which appears in the terms of the matrix \mathbf{A}^C (3.10), is replaced with the longitudinal wave number k_L^C , which is obtained from the dispersion analysis. Similarly, for the case of the transverse wave, the wave number, k^C , is replaced with the transverse wave number k_T^C .

We present the polarization error of DEM associated with the Lagrange multipliers in Figures 9 and 10 versus the angle of orientation, θ , for different values of resolutions. The polarization error is symmetric with respect to $\theta = 45^\circ$, and cyclic around $\theta = 90^\circ$. Except for the case of the longitudinal wave at $\theta = 0^\circ$ and $\nu = 0$, a polarization error exists in all of the cases examined. However, the constraint field exhibits good polarization properties at resolutions larger than 6 points per wavelength for any angle of orientation. Poisson's ratio, ν , has considerable effect on the polarization error for the longitudinal and transverse waves. Unlike the longitudinal waves, the polarization accuracy of the transverse waves improves with the growth of ν .

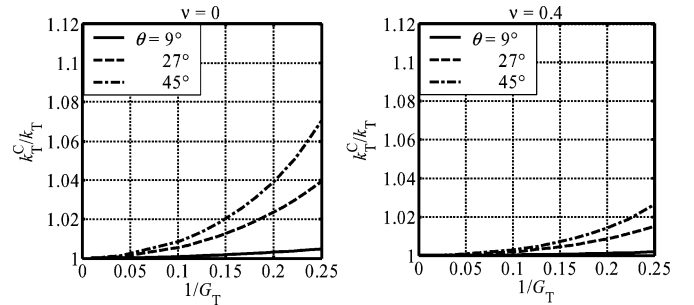


FIG. 8. Convergence rate, transverse phase error of the plane-strain DEM element.

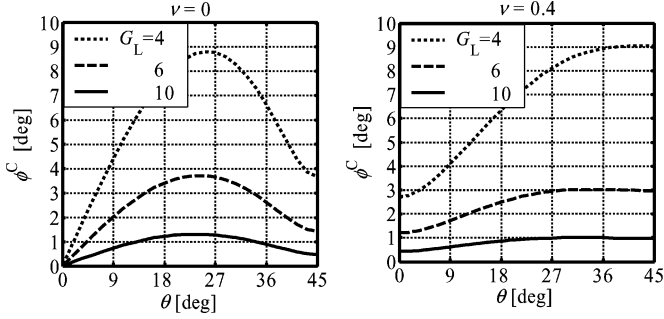


FIG. 9. Polarization error of DEM, longitudinal wave.

We confirm these results by comparison to analytical expressions at the extreme angles. For $\theta = 0^\circ$, the polarization error of the Lagrange multipliers for the longitudinal wave in terms of (3.4) is:

$$\phi^C = \cos^{-1} \left(\frac{2(\tilde{\nu} - 2)a_3 \cos(k_L h/2) - \tilde{\nu}(a_1 + a_2)}{(2(\tilde{\nu}^2 - 2\tilde{\nu} + 2)[(a_1 + a_2)^2 + 4a_3^2 \cos^2(k_L h/2)]^{1/2}} \right). \quad (3.23)$$

For the aforementioned expression, when $\nu = 0$, the following is carried out: $\tilde{\nu} = 2$, $k_T = 2k_L$ and $a_3 = 0$, see (2.8) and (3.5). Also $(a_1 + a_2) < 0$. In this case,

$$\phi^C = \cos^{-1} \left(\frac{-(a_1 + a_2)}{|a_1 + a_2|} \right) = \cos^{-1}(1) = 0, \quad (3.24)$$

independent of resolution. The transverse wave polarization error at $\theta = 0^\circ$ is:

$$\phi^C = \cos^{-1} \left(\frac{a_4 - a_5 + 2 \cos(k_T h/2)}{(2[(a_4 - a_5)^2 + 4 \cos^2(k_T h/2)]^{1/2}} \right). \quad (3.25)$$

Unlike the longitudinal wave, the polarization error of the transverse wave at $\theta = 0^\circ$ is independent of the Poisson's ratio, ν . The results presented in Figures 9 and 10 comply with the analytical solution at this extreme angle.

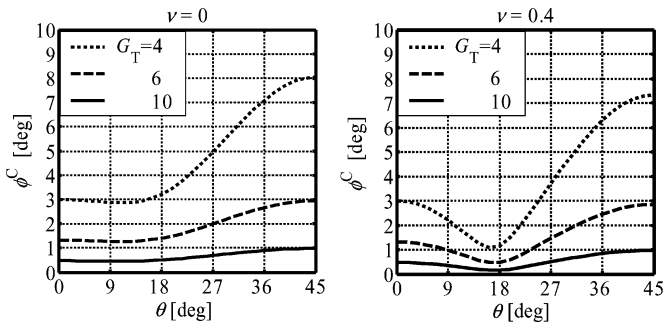


FIG. 10. Polarization error of DEM, transverse wave.

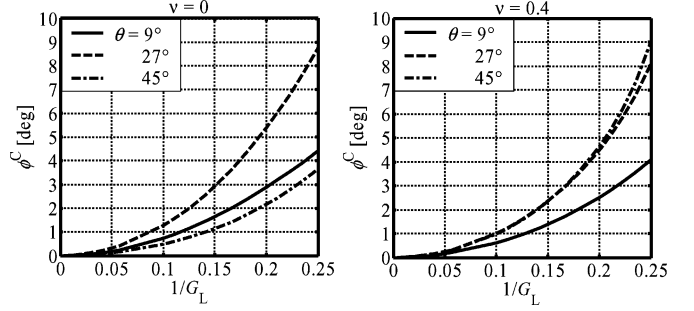


FIG. 11. Convergence rate, longitudinal polarization error of the plane-strain DEM element.

The abovementioned polarization results can be presented by means of convergence rate for the longitudinal and transverse waves as shown in Figures 11 and 12, respectively.

The polarization of the constraint field exhibits good convergence properties even at the largest angular deviation of the mesh relative to the wave (i.e., $\theta = 45^\circ$). For all the examined cases, the polarization is found to be less than 9° for resolutions larger than 4 nodal points per wavelength, and less than 2° for resolutions larger than 10 nodal points per wavelength. The convergence results presented in Figures 11 and 12 correspond to the polarization results presented in Figures 9 and 10.

The dispersion analysis of the basic DEM element considered is carried out on regular meshes. This is usually the case for dispersion analysis, but the results are applicable to computation on general meshes [15, 18, 20, 21, 23, 39]. Dispersion analysis on unstructured meshes was reported recently [5].

4. NUMERICAL EXPERIMENTS

In Section 3, the performance of the DEM basic element for elastic wave problems was examined by plane wave dispersion analysis. We corroborate this dispersion analysis by results of numerical experiments. In the following section we describe these tests and compare the results of the proposed DEM method with those of the standard bilinear Galerkin method.

We consider a problem governed by the homogeneous equation of motion, defined in an $a \times a$ square domain. Inhomogeneous Dirichlet boundary conditions are specified so

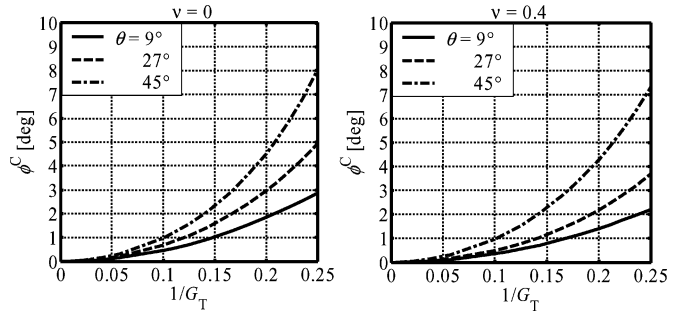


FIG. 12. Convergence rate, transverse polarization error of the plane-strain DEM element.

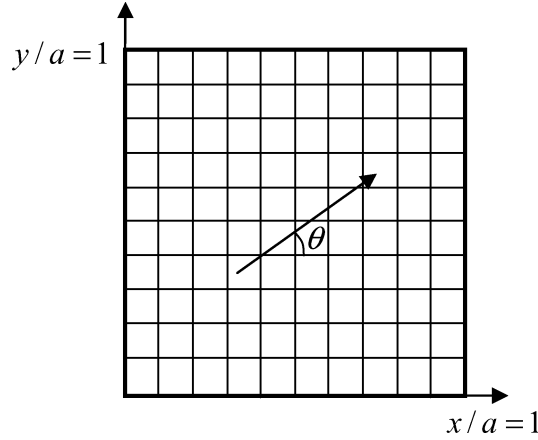


FIG. 13. Problem statement.

that the exact solution is a longitudinal or transverse plane wave propagating in a given direction, θ , see (2.10), (2.11). We examine the accuracy of the described DEM method for various values of the nondimensionalized transverse wave number, $k_T a$, and Poisson's ratio, ν , versus resolution. The domain is discretized by a uniform mesh composed of the plane-strain DEM elements described in this paper. The problem statement is presented in Figure 13.

The wave numbers are selected in order to circumvent resonance, which is related to non-uniqueness of the solution at specific wave numbers.

In order to guarantee the reliability of the numerical results, we verify that the problem being solved does not suffer from ill conditioning. This is verified by checking the condition number of the statically condensed coefficient matrix.

The condition number of the coefficient matrix is presented in Figure 14 versus resolution for different values of Poisson's ratio, ν , and the nondimensionalized wave numbers, $k_T a$. The condition number is expressed in terms of the 2-norm, which is the ratio between the largest to the smallest eigenvalue of this matrix.

The results show that the condition number of the coefficient matrix is smaller than 10^8 for all the cases examined. The double-precision direct solver that is used in the compu-

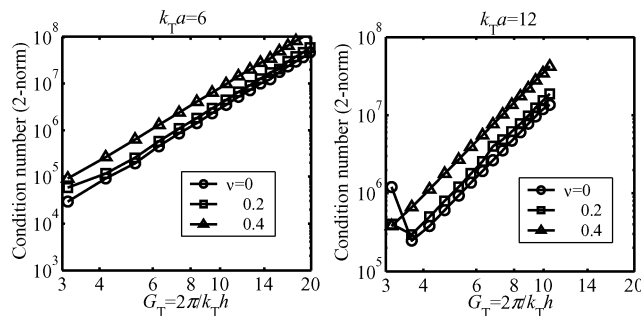
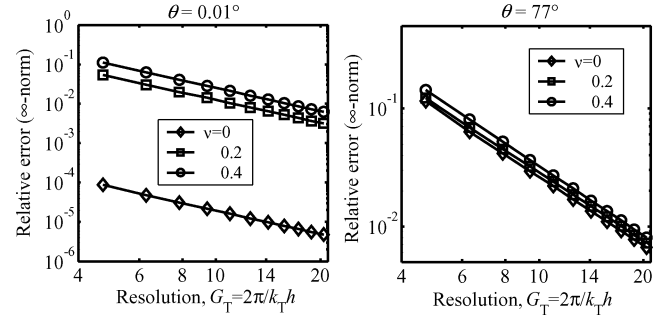


FIG. 14. Condition number of the DEM coefficient matrix.

FIG. 15. Relative nodal error of the displacement, longitudinal wave, $k_T a = 4$.

tations can properly handle linear systems with such condition numbers.

4.1. Numerical Results

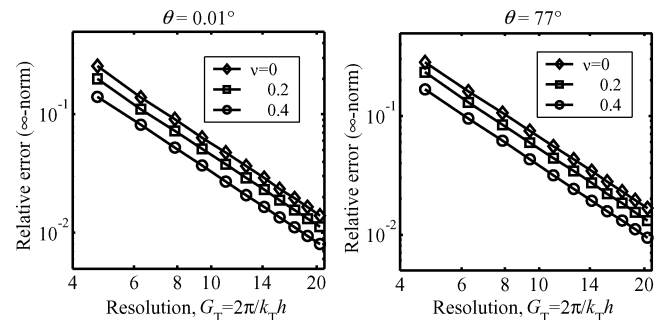
The accuracy of the DEM solution for the displacement field, $\mathbf{u}^h = \mathbf{u}^P + \mathbf{u}^E$, (2.23), is presented in Figure 15 and Figure 16 in terms of the relative error in the nodal ∞ -norm versus resolution. We define the relative error in the ∞ -norm of the nodal solution as follows:

$$\frac{\max_A |\mathbf{u}^h(\mathbf{x}_A) - \mathbf{u}(\mathbf{x}_A)|}{\max_A |\mathbf{u}(\mathbf{x}_A)|}, \quad (4.1)$$

where A is a nodal point.

It should be noted that in the numerical evaluations the direction $\theta = 0.01^\circ$ was used instead of $\theta = 0^\circ$, since the error would drop to zero for a wave aligned with one of the plane waves in the basis.

For all the cases considered, the relative error of the displacement based on the DEM approximation is smaller than 10% for resolutions larger than $G_T = 6$ points per wavelength. This accuracy of DEM is kept, even when the direction of the wave differs significantly from all of the angles of the enrichment ($\theta = 77^\circ$). The accuracy of the numerical solution of the longitudinal wave deteriorates as the Poisson's ratio, ν , increases, while the solution of the transverse wave improves with the

FIG. 16. Relative nodal error of the displacement, transverse wave, $k_T a = 4$.

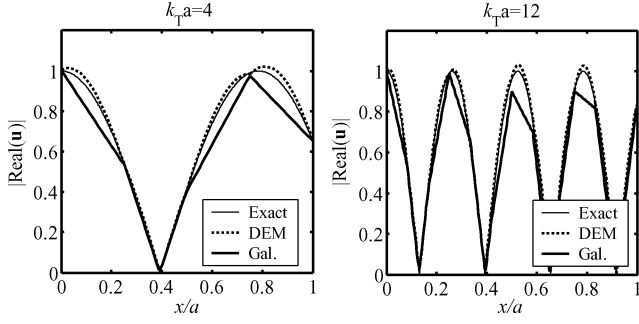


FIG. 17. $|\text{Re}(\mathbf{u})|$ at $y/a = 1/2$, transverse wave, $G_T = 2\pi$, $\nu = 0.3$, $\theta = 0.01^\circ$.

growth of ν . The most accurate solution is obtained in the case of the longitudinal wave at $\theta = 0.01^\circ$ and $\nu = 0$. The dependence of the numerical solution on the Poisson's ratio, ν , complies with the results of the dispersion analysis and the polarization error of DEM, presented in Section 3.2.3. There we show that the dispersion behavior of the longitudinal waves deteriorates as ν increases, while the transverse dispersion improves with the growth of ν . Furthermore, the smallest polarization error occurs for the case of the longitudinal wave at $\theta = 0.01^\circ$ and $\nu = 0$.

Later in this section, we will show that this accuracy of DEM remains even if the wave number increases.

We compare the results of the proposed DEM method with the accuracy of the standard Galerkin method. Figure 17 shows an example of solutions obtained at the middle of the domain ($y/a = 1/2$).

The nodal error of the Galerkin solution increases with the growth of the frequency although the resolution is kept constant. This is the pollution error (see Section 1). In comparison, the DEM method exhibits good nodal accuracy and low pollution even at relatively low resolution (e.g., $G = 2\pi$ points per wavelength). Moreover, no considerable jump in the DEM nodal solution is observed, despite the fact that the solution is discontinuous, and the continuity is only weakly enforced.

The accuracy of DEM, compared with the standard Galerkin, is presented in Figures 18 and 19, in terms of the relative error in the nodal ∞ -norm versus resolution, at $\nu = 0.3$. For both the low and high frequencies considered, DEM shows noticeable

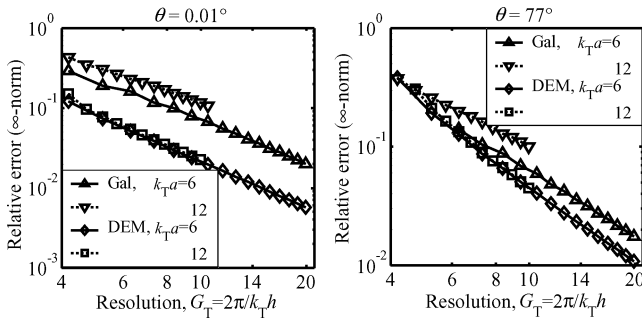


FIG. 18. Relative nodal error of the displacement, longitudinal wave, $\nu = 0.3$.

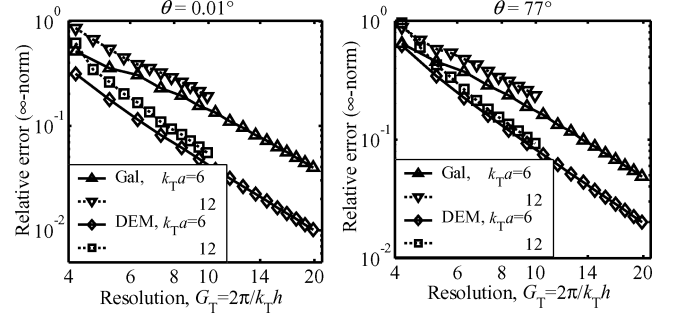


FIG. 19. Relative nodal error of the displacement, transverse wave, $\nu = 0.3$.

accuracy advantage over the standard Galerkin method. As the frequency increases, the DEM solution becomes more accurate by almost an order of magnitude compared with the standard Galerkin solution. This main difference occurs when the mesh is almost aligned with the wave ($\theta = 0.01^\circ$).

Unlike the Galerkin solution, DEM exhibits relatively low pollution for any of the cases considered (the error of DEM appears to depend mostly on resolution and not on $k_T a$ itself). The advantage of DEM in the aspect of low pollution compared with the standard Galerkin method is kept, even when the direction of the wave differs significantly from all of the angles of the enrichment ($\theta = 77^\circ$). However, the accuracy advantage of DEM over the standard Galerkin method at $\theta = 77^\circ$ is less significant.

Next, we present the accuracy of DEM in the context of the Lagrange multipliers, which are related to the boundary traction. The exact boundary traction is based on (2.12). We compare the solution of the Lagrange multipliers with the exact value of the boundary traction at the middle of the element edges. The accuracy of the constraint field is presented in Figures 20 and 21 in terms of the relative error in the ∞ -norm versus resolution at $\nu = 0.3$.

The behavior of the Lagrange multipliers is similar to the behavior of the displacement solution of DEM presented in Figure 18 and Figure 19. It appears that for a given resolution, a similar relative error occurs for both the Lagrange multipliers and the displacement at all the cases considered. Like the displacement

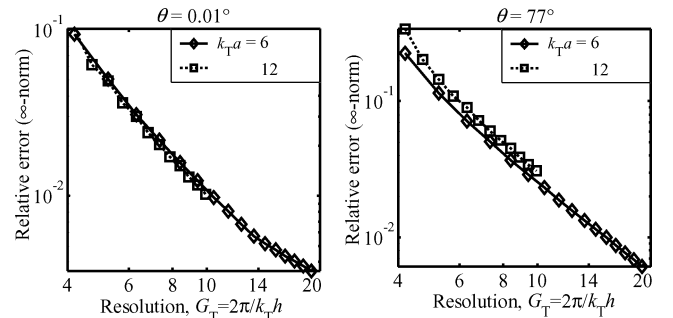


FIG. 20. Relative error of the constraint field, longitudinal wave, $\nu = 0.3$.

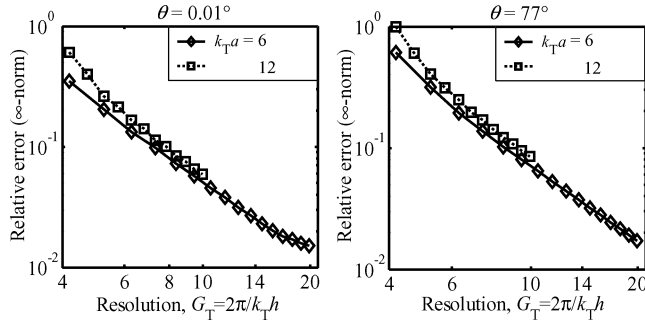


FIG. 21. Relative error of the constraint field, transverse wave, $\nu = 0.3$.

solution, the constraint field also exhibits low pollution at any angle of orientation considered. This similarity in behavior supports the claim that the performance of the DEM element is represented by the properties of the Lagrange multipliers (see Section 3.2.1).

4.2. Computational Cost

Due to the element-level static condensation, the computational cost of the described method based on the plane-strain DEM element is virtually independent of the number of elastic waves of which each element consists. The computational cost is governed by the total number of Lagrange multipliers and the polynomial degrees of freedom. We consider a problem in a square domain, discretized by a uniform mesh of $n \times n$ elements. Such a mesh has $(n + 1)^2$ vertices and $2n(n + 1)$ edges. The statically condensed plane-strain DEM elements require $2(n + 1)^2$ vertex degree of freedom and $4n(n + 1)$ edge degree of freedom. The asymptotic number of degrees of freedom ($n \gg 1$) for the standard Galerkin method is $2n^2$. On the other hand, the number of degrees of freedom of the described plane-strain DEM method is $6n^2$ (i.e., $2n^2$ nodal + $4n^2$ edge). Consequently, the DEM method requires asymptotically twice more degrees of freedom than the standard Galerkin method. This requirement is valid either for the considered elastic problem or the acoustic problem, see [9].

5. CONCLUSIONS

A finite element formulation for the Discontinuous Enrichment Method (DEM) for plane-strain elastic waves is presented and analyzed. DEM in the context of the elastic problem is formulated as follows: The standard finite element polynomial field is enriched by eight vector-valued longitudinal and transverse plane waves aligned with the axes. The plane waves, which are discontinuous enrichment functions, are free-space solutions of the isotropic, homogeneous equation of motion. Continuity of the numerical solution across element boundaries and Dirichlet boundary conditions are weakly enforced by Lagrange multipliers. The Lagrange multipliers are associated with the boundary traction that enforces the continuity of the displacement field. The traction varies along each element boundary for the enrich-

ment functions considered. Nevertheless, the Lagrange multipliers are approximated by piecewise constants along the element sides. Due to the discontinuous nature of the enrichment, it is eliminated from the formulation by static condensation on the element level prior to assembly. Elimination of the enrichment field leads to a simpler formulation. The condensed problem is then expressed in terms of the polynomial field and the Lagrange multipliers. The enrichment within each element is recovered after the solution.

The dispersion analysis of phase and polarization errors demonstrated the good performance of the plane-strain DEM element. We corroborated the dispersion analysis by results of numerical experiments, and presented a correlation between the performance of the Lagrange multipliers and the quality of the displacement solution. The numerical results were compared with the standard Galerkin method. For high frequency of plane wave propagation, DEM was proven to be better than the standard Galerkin FEM by almost an order of magnitude. The best performance of the described DEM element occurs in approximation of the waves propagating at angles close to the directions of the enrichment waves. However, good performance was achieved even when the direction of the wave differs significantly from all of the angles of the enrichment. The enriched method exhibits very low pollution in contrast to the Galerkin method.

Our work indicates the potential value of DEM for cases of high frequency elasto-dynamic problems, in which standard finite element methods are inadequate.

ACKNOWLEDGMENTS

The authors wish to thank Paul Barbone, RenGanel, Eran Grosu, Shimon Shmulman and Vitaly Skralivetsky for helpful discussions.

REFERENCES

1. N.N. Abboud, P.M. Pinsky, Finite Element Dispersion Analysis for the Three-Dimensional Second-order Scalar Wave Equation, *Int. J. Numer. Methods Engrg.*, vol. 35, pp. 1183–1218, 1992.
2. I. Babuška, F. Ihlenburg, E.T. Paik, S.A. Sauter, A Generalized Finite Element Method for Solving the Helmholtz Equation in Two Dimensions with Minimal Pollution, *Comput. Methods Appl. Mech. Engrg.*, vol. 128, pp. 325–359, 1995.
3. I. Babuška, J.M. Melenk, The Partition of Unity Method, *Int. J. Numer. Methods Engrg.*, vol. 40, pp. 727–758, 1997.
4. A. Bayliss, C.I. Goldstein, E. Turkel, On Accuracy Conditions for the Numerical Computation of Waves, *J. Comput. Phys.*, vol. 59, no. 3, pp. 396–404, 1985.
5. P.E. Bernard, E. Deleersnijder, V. Legat, J.F. Remacle, Dispersion Analysis of Discontinuous Galerkin Schemes Applied to Poincaré, Kelvin and Rossby Waves, *J. Sci. Comput.*, vol. 34, pp. 26–47, 2008.
6. P. Bettess, Short-Wave Scattering: Problems and Techniques, *Phil. Trans. R. Soc. Lond. A*, vol. 362, pp. 421–443, 2004.
7. P. Bettess, J. Shiron, O. Laghrouche, B. Peseux, R. Sugimoto, J. Trevelyan, A Numerical Integration Scheme for Special Finite Elements for the Helmholtz Equation, *Int. J. Numer. Methods Engrg.*, vol. 56, no. 4, pp. 531–552, 2002.

8. J.D. De Basabe, M.K. Sen, Grid Dispersion and Stability Criteria of Some Common Finite-Element Methods for Acoustic and Elastic Wave Equations, *Geophysics*, vol. 72, no. 6, pp. T81–T95, 2007.
9. C. Farhat, I. Harari, L.P. Franca, The Discontinuous Enrichment Method, *Comput. Methods Appl. Mech. Engrg.*, vol. 190, pp. 6455–6479, 2001.
10. C. Farhat, I. Harari, U. Hetmaniuk, The Discontinuous Enrichment Method for Multiscale Analysis, *Comput. Methods Appl. Mech. Engrg.*, vol. 192, pp. 3195–3210, 2003.
11. L.P. Franca, C. Farhat, Bubble Functions Prompt Unusual Stabilized Finite Element Methods, *Comput. Methods Appl. Mech. Engrg.*, vol. 123, pp. 299–308, 1995.
12. R. Ganel, Development of the GLS Finite Element Method for Time Harmonic Elastic Waves, M.Sc. Thesis, Tel-Aviv University, Tel-Aviv, Israel, 2006.
13. I. Goldstein, The Weak Element Method Applied to Helmholtz Type Equations, *Appl. Numer. Math.*, vol. 2, pp. 409–426, 1986.
14. G.H. Golub, C.F. Van Loan, *Matrix Computations*, 3rd edition, Johns Hopkins, Baltimore, MD, 1996.
15. E. Grosu, I. Harari, Studies of the Discontinuous Enrichment Method for Two-Dimensional Acoustics, *Finite Elements in Analysis and Design*, vol. 44, no. 5, pp. 272–287, 2008.
16. I. Harari, A Survey of Finite Element Methods for Time-Harmonic Acoustics, *Comput. Methods Appl. Mech. Engrg.*, vol. 195, pp. 1594–1607, 2006.
17. I. Harari, C. Farhat, U. Hetmaniuk, Multiple-stencil Dispersion Analysis of the Lagrange Multipliers in a Discontinuous Galerkin Method for the Helmholtz Equation, *J. Comput. Acoust.*, vol. 11, no. 2, pp. 239–254, 2003.
18. I. Harari, K. Gosteev, Bubble-based Stabilization for the Helmholtz Equation, *Int. J. Numer. Methods Engrg.*, vol. 70, no. 10, pp. 1241–1260, 2007.
19. I. Harari, S. Haham, Improved Finite Element Methods for Elastic Waves, *Comput. Methods Appl. Mech. Engrg.*, vol. 166, pp. 143–164, 1998.
20. I. Harari, F. Magoulès, Numerical Investigations of Stabilized Finite Element Computations for Acoustics, *Wave Motion*, vol. 39, no. 4, pp. 339–349, 2004.
21. I. Harari, C.L. Nogueira, Reducing Dispersion of Linear Triangular Elements for the Helmholtz Equation, *J. Engrg. Mech.*, vol. 128, no. 3, pp. 351–358, 2002.
22. I. Harari, Z. Shohet, On Non-reflecting Boundary Conditions in Unbounded Elastic Solids, *Comput. Methods Appl. Mech. Engrg.*, vol. 163, pp. 123–139, 1998.
23. I. Harari, R. Tezaur, C. Farhat, A Study of Higher-order Discontinuous Galerkin and Quadratic Least-squares Stabilized Finite Element Computations for Acoustics, *J. Comput. Acoust.*, vol. 14, no. 1, pp. 1–19, 2006.
24. T.J.R. Hughes, Multiscale Phenomena: Green's Functions, the Dirichlet-to-Neumann Formulation, Subgrid Scale Models, Bubbles and the Origins of Stabilized Methods, *Comput. Methods Appl. Mech. Engrg.*, vol. 127, pp. 387–401, 1995.
25. T.J.R. Hughes, *The Finite Element Method — Linear Static and Dynamic Finite Element Analysis*, Dover, New York, 2000.
26. T.J.R. Hughes, G.R. Feijóo, L. Mazzei, J.B. Quincy, The Variational Multiscale Method — A Paradigm for Computational Mechanics, *Comput. Methods Appl. Mech. Engrg.*, vol. 166, pp. 3–24, 1998.
27. T. Huttunen, J.P. Kaipio, P. Monk, An Ultra-weak Method for Acoustic Fluid-solid Interaction, *J. Comput. Appl. Math.*, vol. 213, no. 1, pp. 166–185, 2008.
28. T. Huttunen, P. Monk, F. Collino, J.P. Kaipio, The Ultra-weak Variational Formulation for Elastic Wave Problems, *SIAM J. Sci. Comput.*, vol. 25, no. 5, pp. 1717–1742, 2004.
29. F. Ihlenburg, *Finite Element Analysis of Acoustic Scattering*, Springer-Verlag, New York, 1998.
30. F. Ihlenburg, I. Babuška, Finite Element Solution of the Helmholtz Equation with High Wave Number. Part I: The h -Version of the FEM, *Computers Math. Applic.*, vol. 30, pp. 9–37, 1995.
31. P. Ladevéze, H. Riou, Calculation of Medium-frequency Vibrations over a Wide Frequency Range, *Comput. Methods Appl. Mech. Engrg.*, vol. 194, pp. 3167–3191, 2005.
32. O. Laghrouche, P. Bettess, Short Wave Modeling Using Special Finite Elements, *J. Comput. Acoust.*, vol. 8, pp. 189–210, 2000.
33. O. Laghrouche, P. Bettess, D. Le Houédec, *Special Finite Elements for High Frequency Elastodynamic Problems: First Numerical Experiments*, Civil-Comp Press, Stirling, Scotland, 2001.
34. K.J. Marfurt, Accuracy of Finite-difference and Finite-element Modeling of the Scalar and Elastic Wave Equations, *Geophysics*, vol. 49, no. 5, pp. 533–549, 1984.
35. P. Massimi, R. Tezaur, C. Farhat, A Discontinuous Enrichment Method for Three-dimensional Multiscale Harmonic Wave Propagation Problems in Multi-fluid and Fluid-solid Media, *Int. J. Numer. Methods Engrg.*, vol. 76, no. 3, pp. 400–425, 2008.
36. E. Perrey-Debain, J. Trevelyan, P. Bettess, P-wave and S-wave Decomposition in Boundary Integral Equation for Plane Elastodynamic Problems, *Commun. Numer. Methods Engrg.*, vol. 19, no. 12, pp. 945–958, 2003.
37. S.F. Li, A. Gupta, X.H. Liu, M. Mahyari, Variational Eigenstrain Multiscale Finite Element Method, *Comput. Methods Appl. Mech. Engrg.*, vol. 193, pp. 1803–1824, 2004.
38. S. Shmulman, Dispersion Analysis of the Discontinuous Enrichment Method for Acoustic Problems, M.Sc. Thesis, Tel Aviv University, Tel Aviv, Israel, 2003.
39. J.R. Stewart, T.J.R. Hughes, h -Adaptive Finite Element Computation of Time-harmonic Exterior Acoustics Problems in Two Dimensions, *Comput. Methods Appl. Mech. Engrg.*, vol. 146, no. 1–2, pp. 65–89, 1997.
40. R. Tezaur, L. Zhang, C. Farhat, A Discontinuous Enrichment Method for Capturing Evanescent Waves in Multiscale Fluid and Fluid/solid Problems, *Comput. Methods Appl. Mech. Engrg.*, vol. 197, no. 19, pp. 1680–1698, 2008.
41. L. Zhang, R. Tezaur, C. Farhat, The Discontinuous Enrichment Method for Elastic Wave Propagation in the Medium-frequency Regime, *Int. J. Numer. Methods Engrg.*, vol. 66, no. 13, pp. 2086–2114, 2006.